



Multiple source downwellings beneath eastern North China revealed by 3-D CCP migration of receiver function data

Jiahui Zuo^a, Liwei Wang^a, Fenglin Niu^{a,b,*}

^a State Key Laboratory of Petroleum Resources and Prospecting, and Unconventional Petroleum Research Institute, China University of Petroleum Beijing, Beijing 102249, China

^b Department of Earth, Environmental and Planetary Sciences, Rice University, Houston, TX 77005, USA

ARTICLE INFO

Keywords:

Mantle discontinuities
Phase transition
Receiver function
North China
Delamination and Subduction

ABSTRACT

We collected and processed a total of 97,700 teleseismic receiver functions recorded by 580 broadband seismic stations from 686 earthquakes to study the mantle transition zone beneath eastern North China. We employed a recently developed 3-D P- and S-wave velocity model (the East Asia Radially Anisotropic Model, EARA2014) to compute *Pds* moveouts to migrate receiver function data. Amplitudes of the stacked *P660s* and *P410s* using the 3-D *Pds* moveout table are approximately 30% higher than those calculated from the 1-D iasp91 model. The 3-D volume of CCP (common-conversion-point) stacked images that covers the area of 110–125°E and 36–43°N revealed two remarkable mantle transition zone anomalies with significant depression of the 660-km discontinuity. Together with other seismic observations, we speculated that these two anomalies are resulted from two different dynamic processes beneath eastern North China.

1. Introduction

The North China Craton (NCC) formed in the Archean is one of the oldest continental cratons in the world. It is bound with the Xing-Meng Block to the north by the Central Asian Orogenic Belt, and with the Yangtze Block to the south by the Qinling-Dabie Belt (Fig. 1a). Tectonically, the craton consists of an active eastern block (ENCC) and an inactive western block (WNCC), which are separated by the Central Orogenic Belt (Fig. 1a). Global tomography studies (e.g., [Megnin and Romanowicz, 2000](#); [Grand, 2002](#)) showed that the ENCC and the Yangtze craton to the south are the only large ancient cratons on Earth that do not have high shear velocity roots beneath them. Meanwhile, geochemical studies of xenoliths in ENCC found that the kimberlite pipes and basalts, which brought the xenoliths to the surface, erupted during two distinct time periods, first during the Ordovician and then later from the Mesozoic through the Tertiary ([Menzies et al., 1993](#); [Griffin et al., 1998](#); [Gao et al., 2002](#)). The Ordovician garnet peridotite xenoliths indicated that the craton had a typical depleted, cool Archean root to a depth near 200 km at ~400 Ma ([Griffin et al., 1998](#)). In contrast, abundant spinel lherzolite xenoliths brought up in Tertiary to Quaternary basalts showed a hot and relatively undepleted mantle across the ENCC ([O'Reilly et al., 2001](#)). These observations have led to the hypothesis that the mantle cratonic root has been removed beneath

at least the ENCC ([Menzies et al., 1993](#); [Griffin et al., 1998](#); [Gao et al., 2002](#)), which is consistent with the global tomographic images. The xenolith sites are, however, spatially restricted; they could be special places where the cratonic lithosphere was displaced. The lateral and depth resolutions of the global tomographic models are also greatly limited; therefore it is unclear on the lateral extent of the removal of the cratonic lithosphere beneath ENCC.

Since the Mesozoic, the craton has undergone massive extension, which is likely caused by its interaction with subduction to the east – a situation similar to what has occurred in the western United States during the Cenozoic. The subduction is also attributed to have caused the removal of the cratonic keel beneath ENCC ([Windley et al., 2010](#); [Wang et al., 2016](#)), although details on the subduction-induced removal are still debated ([Zhu et al., 2012a](#)), partly because there is a lack of knowledge about the slab geometry beneath ENCC. Early studies of P-wave traveltimes tomography ([Fukao et al., 1992, 2001](#); [Huang and Zhao, 2006](#)) revealed a large-scale high-velocity anomaly in the mantle transition zone beneath a large portion of the ENCC. This high-velocity anomaly was interpreted as the stagnated Pacific slab that lies horizontally after it enters into the transition zone. Recent finite-frequency traveltimes and waveform tomography studies (e.g., [Obayashi et al., 2013](#); [Tang et al., 2014](#); [Chen et al., 2015](#); [Tao et al., 2018](#)), however, found that the geometry of the high-velocity anomalies inside the

* Corresponding author at: State Key Laboratory of Petroleum Resources and Prospecting, and Unconventional Petroleum Research Institute, China University of Petroleum Beijing, Beijing 102249, China.

E-mail address: niu@rice.edu (F. Niu).

<https://doi.org/10.1016/j.jseaes.2020.104266>

Received 10 October 2019; Received in revised form 31 January 2020; Accepted 1 February 2020

Available online 03 February 2020

1367-9120/ © 2020 Elsevier Ltd. All rights reserved.

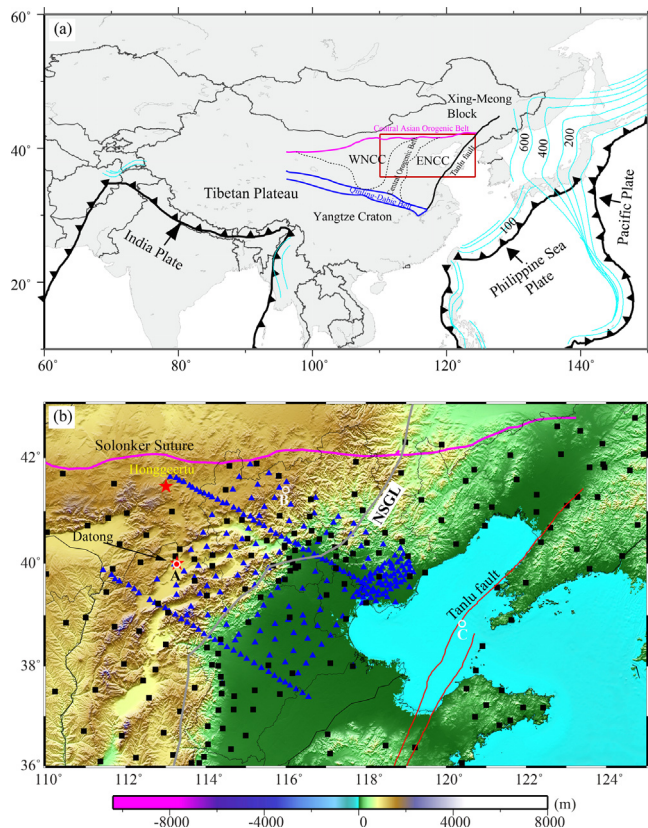


Fig. 1. Maps show the major tectonic setting of China and its surrounding areas (a) and the topography of North China (b). Arrows in (a) indicate the subduction of the Pacific and Philippine plates, and the collision of the Indian plate on the east and southwest sides of China, respectively. The red rectangular region shows the location of the study area. Green lines indicate the descending Pacific, Philippine and Indian plates. Blue solid lines outline the Qinling-Dabie orogenic belt, and the pink solid line represents the Solonker suture that separates the Central Asian Orogenic Belt and the North China Craton. ENCC and WNCC are the eastern and western North China Craton bounded by the Central Orogenic Belt. (b) Blue triangles and black squares indicate broadband seismic stations of the temporal NCArray and the permanent CEArray, respectively. The grey, pink and red lines represent the North South Gravity Lineament (NSGL), the Solonker suture and the Tanlu fault system, respectively. The two red stars indicate the Honggeertu and Datong volcanic fields, respectively. The three white circles labeled A, B and C show the locations whose depth P-to-S conversion profiles are shown in Fig. 4c, d, and e, respectively. (For interpretation of the references to color in this figure legend, the reader is referred to the web version of this article.)

mantle transition zone beneath ENCC is rather complicated, suggesting a complicated subduction history beneath the area.

In addition to seismic tomography, receiver function imaging has been used to identify cold slabs through mapping their induced topography at the 410-km and 660-km seismic discontinuities, which define the upper and lower boundaries of the mantle transition zone. The two seismic discontinuities are associated with the olivine-to-wadsleyite phase transition (Katsura and Ito, 1989) and the post-spinel transformation (Ito and Takahashi, 1989), respectively. Both phase transitions are temperature sensitive, meaning that the two seismic discontinuities are expected to occur at different depths within a cold descending slab. Chen and Ai (2009) migrated a large amount of receiver function data recorded in North China and found that the depth to the 660-km discontinuity changes rapidly across the North South Gravity Lineament (NSGL), and the mantle transition zone located at the east side of the NSGL is ~ 10 – 20 km thicker than it is in the west. They interpreted the thickened mantle transition zone beneath ENCC to be caused by the stagnant Pacific slab that spread widely in the area, as shown in

the travel time tomographic models (Huang and Zhao, 2006). Wang and Niu (2011) confirmed the broad depression of the 660-km beneath eastern China. However, there are still significant differences in the imaged depths of the two discontinuities between the two studies.

One potential source for the discrepancy is the reference velocity model employed in the time-to-depth conversion (Guan and Niu, 2018). Niu and Kawakatsu (1998) computed the time offsets of the P-to-S converted waves at the 660-km discontinuity ($P660s$) using the iasp91 model (Kennett and Engdahl, 1991) and the 1-D model of the tectonically active North America (Grand and Helmberger, 1984; Walck, 1984). They found a traveltime difference of nearly 2 s, which converts to 20 km in depth. In other words, the depth of the 660 km beneath the tectonically active North America can be overestimated by ~ 20 km if the iasp91 model is used as the reference model. Accurately computing Pds time offsets requires 3-D reference velocity models that have similar resolutions of both P and S waves, which are difficult to obtain from traveltime tomography due to the differences in the quality and quantity of P- and S-wave picks in earthquake catalogs. Recent success in full waveform seismic tomography allows developing high-resolution S-wave models by naturally integrating body and surface wave data (Zhu et al., 2012b; Chen et al., 2015; Tao et al., 2018). In this study, we employed the East Asia Radially Anisotropic Model (EARA2014, Chen et al., 2015) to compute Pds time offsets and then applied a common-conversion-point (CCP) stacking analysis to a large receiver function dataset that samples the ENCC and its surrounding areas. We found that the amplitude of $P410s$ and $P660s$ increases by approximately 30% when the EARA2014 Pds time moveouts were employed in the stacking, suggesting it is a better reference model than the 1-D iasp91 model. There are also significant differences in the imaged depths with the two models. The 3-D CCP stacked image of the mantle transition zone revealed multiple downwellings beneath the study area that are likely associated with different types of tectonic events.

2. Data and analysis

2.1. NCArray and CEArray

We used teleseismic waveform data recorded by the dense temporal North China Array (blue triangles in Fig. 1b) and the permanent China Digital Seismic Network (CDSN, black squares in Fig. 1b) operated by the China Earthquake Administration (CEA). Hereafter we refer the temporal array as the NCArray and the CEA permanent array as the CEArray, respectively. The NCArray was deployed by the Institute of Geophysics at CEA between October of 2006 and July of 2009 (e.g., Fang et al., 2009; Lu et al., 2009). The 580 stations of the two arrays provided a good coverage of eastern North China, including a large part of the Bohai Sea, the Taihang and Yanshan mountain ranges (Fig. 1b). Station spacing varies from ~ 10 km along two dense survey lines of the NCArray to 100 km among the CEArray stations. Most of the NCArray stations are equipped with a Guralp CMG-3ESPC seismometer and a Reftek 130 digital acquisition system, while the CEArray stations are mixtures of seven types of sensors and digitizers (Zheng et al., 2009).

We visually examined all the teleseismic data within the epicentral distance range of 30° – 90° from earthquakes with a magnitude ≥ 5.5 occurring between 10/2006 and 07/2010. We chose a total of 686 earthquakes that were well recorded by either the NCArray or CEArray, or both. The coverage from these earthquakes was reasonably good in both distance and azimuth (Fig. 2).

2.2. Receiver functions

Niu and Li (2011) found a significant portion of the CEArray stations had problems in orientation. Therefore we first applied their method that employs the P-wave particle motion in the period band of 5–50 s to estimate the true orientations of all the stations. Next, based on the estimated component azimuths we rotated the two horizontal

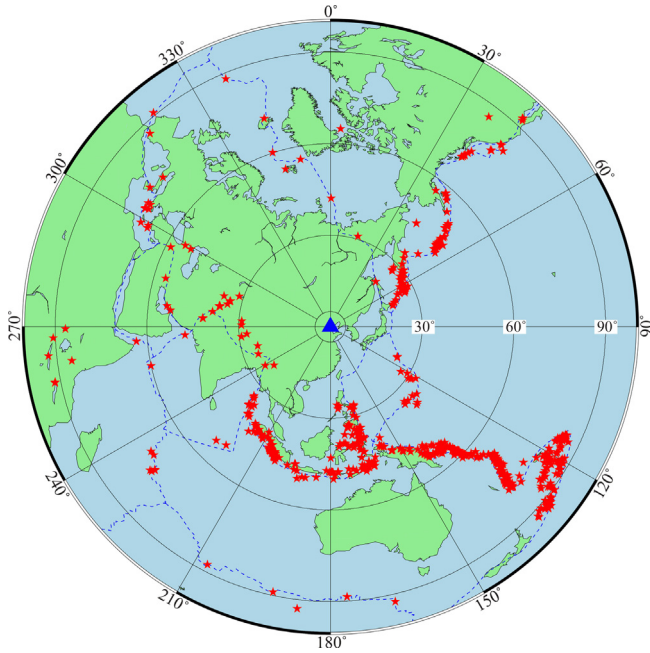


Fig. 2. An azimuthal map projection shows the 686 earthquakes (red stars) used in this study. The blue triangle indicates the center of the study area, and the three circles indicate angular distances of 30°, 60°, and 90°, respectively. Note that although the earthquakes appear to be ~20–100° away from the center, we only chose station-earthquake pairs in the epicentral distance range of 30° to 90°. (For interpretation of the references to color in this figure legend, the reader is referred to the web version of this article.)

components of the seismograms into the radial (R) and transverse (T) components. For each teleseismic record, we then computed the 2-D covariance matrix using the vertical (Z) and radial components of the direct P waves, and further obtained the two eigenvectors of the 2-D covariance matrix. The eigenvector with the larger eigenvalue is expected to be the P-wave particle motion, which is the longitudinal direction and referred to as P direction hereafter. We further refer the other eigenvector direction as the in-plane transverse direction, denoted as the SV-direction. The Z-R components were further rotated to the P and SV directions, which correspond to the two principal directions of the 2-D covariance matrix. Lastly, we computed the receiver functions by deconvolving the P-component records from SV-component records (Vinnik, 1977; Niu and Kawakatsu, 1998; Niu et al., 2005).

We employed the “water level” technique (Clayton and Wiggins, 1976) to perform the deconvolution in the frequency domain:

$$RF(\omega) = \frac{SV(\omega) \cdot P^*(\omega)}{\max\{|P(\omega)|^2, k \cdot |P_{\max}(\omega)|^2\}} e^{-\frac{\omega}{2a}}. \quad (1)$$

Here $RF(\omega)$ represents the receiver function in the frequency domain, and ω is the angular frequency. k and a are two constants that define “water level” and the corner frequency of the Gaussian low pass filter, which were set to 0.01 and 1.5, respectively. $a = 1.5$ is roughly equivalent to a corner frequency of 0.5 Hz. $P(\omega)$ and $SV(\omega)$ are the spectra of the P and SV components, and $|P_{\max}(\omega)|^2$ refers to the maximum amplitude of the P-component power spectrum. To satisfy the causality of linear convolution, we employed two different time windows in computing $P(\omega)$ and $SV(\omega)$. We used a 100-s time window (5 s and 95 s before and after the P wave) and a 250-s time window (50 s and 200 s before and after the P wave) to compute $P(\omega)$ and $SV(\omega)$, respectively. We further screened receiver functions with various methods (Chen et al., 2010) to eliminate noisy data. The total number of receiver functions used in the CCP imaging is 97,700.

2.3. CCP gathering with 1-D and 3-D Pds traveltimes

We applied the CCP stacking technique to the receiver-function data to image the 410-km and 660-km discontinuities and their lateral variations beneath eastern North China (e.g., Dueker and Sheehan, 1997; Niu et al., 2005; Wang and Niu, 2011). The CCP stacking technique assumes that the teleseismic P coda consists of P-to-S conversion (Pds) waves and employs the Pds moveouts to convert coda time to conversion depth. Hence it is not a true migration, and is expected to image relatively flat structures, such as the 410-km and 660-km discontinuities. For each receiver function, we first constructed a table that contains the 1-D relative travel times and geographic locations of the P-to-S conversions at a set of grids (d) in the depth range of 300 to 800 km. This was done by raytracing the Pds and direct P waves using the 1-D iasp91 velocity model (Kennett and Engdahl, 1991) and the depth grid interval was set to 1 km.

To compute the 3-D Pds moveouts, we first projected the above 1-D Pds raypaths into the $50 \text{ km} \times 50 \text{ km} \times 50 \text{ km}$ blocks of the 3-D EARA2014 (Chen et al., 2015) model and computed the segment traveltimes in each block. We then calculated the segment traveltime perturbations in each block along the 1-D ray paths using the 3-D P- and S-wave velocities of the EARA2014 model. The traveltimes perturbations were summed to obtain the 3-D Pds travel times, and the 3-D moveouts were computed by subtracting them from the 3-D P wave traveltimes, which were also computed by adding the 3-D corrections to the 1-D iasp91 traveltimes. We also included a 3-D crustal correction using the method of Liu et al. (2015) in the 3-D Pds moveout table. More specifically, the crustal correction was scaled from the Moho P_s time residual with respect to the iasp91 model:

$$t_c = \left(1 - \frac{K_m}{K_c}\right) (t_{Ps}^{obs} - t_{Ps}^{iasp91}), \quad \text{where } K_m = \frac{\cos \theta_m}{\beta_m} - \frac{\cos \phi_m}{\alpha_m}; K_c = \frac{\cos \theta_c}{\beta_c} - \frac{\cos \phi_c}{\alpha_c}. \quad (2)$$

Here (α_m, β_m) and (α_c, β_c) are the P- and S-wave velocities of the uppermost mantle and crust, respectively, and (θ_m, ϕ_m) and (θ_c, ϕ_c) are their corresponding incident angles. K_m and K_c are 0.103 and 0.122, respectively, for a teleseismic event with an epicentral distance of 60° and a focal depth of 0 km, resulting in a scaling factor of ~0.156 (Liu et al., 2015). Since the Moho P_s time residuals are in the range of -1.31 s to 1.99 s, the overall corrections from the 3-D crustal structure including topography are insignificant.

We divided the study area (36°N to 43°N, 110°E to 125°E) into meshed grids of 0.2° by 0.2°, and used a circular cap with a radius of 1 degree for gathering the receiver functions, resulting in a total of 2736 (36 × 76) caps. This parameterization led to large overlapping among the caps, which served as lowpass filtering of the topographic relief on the two discontinuities with a corner wavelength roughly equivalent to the size of the caps, 200 km in diameter. In each cap, we summed the receiver functions with their Pds conversion points located inside the cap based on the 3-D Pds moveout. Instead of adding the single value recorded at the closest sampling point to the Pds moveout, we took a 0.2-second long window centered on the moveout from each receiver function, stacked them, and took the average value of the stacked receiver function as the Pds conversion coefficient.

We employed an N^{th} -root stacking technique (Muirhead, 1968) to stack receiver functions. For the i^{th} cap, let $r_k(t)$ represents the k^{th} receiver function gathered in the cap, and t_{dk} is the 1-D or 3-D Pds arrival time for a hypothetical discontinuity at depth d , and an N^{th} -root stack, $R(d)$, is given by

$$R_i(d) = y_i(d) |y_i(d)|^{N-1} \quad (3)$$

where

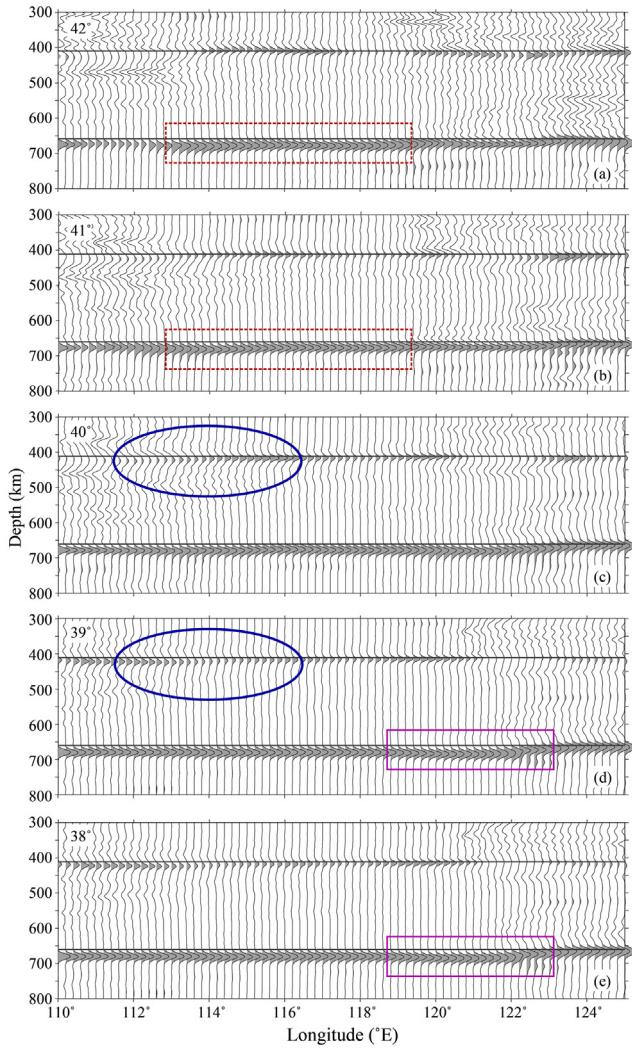


Fig. 3. Depth sections of the 3-D CCP gathered receiver functions along latitude 42°N (a), 41°N (b), 40°N (c), 39°N (d), and 38°N (e). The two horizontal black lines indicate depths of 410 km and 660 km, respectively. The red dotted rectangular shown in (a) and (b), the blue solid ellipse shown in (c) and (d), and the pink solid rectangular shown in (d) and (e) denote the northern Yanshan mountain range (NY) transition zone anomaly, the Datong volcanic region, and the Bohai Sea (BS) transition zone anomaly, respectively. (For interpretation of the references to color in this figure legend, the reader is referred to the web version of this article.)

$$y_i(d) = \frac{1}{K} \sum_{k=1}^K w_k \text{sign}(r_k(t_{dk})) |r_k(t_{dk})|^{1/N} \quad (4)$$

Here K is the total number of receiver functions gathered at the i^{th} cap. w_k is a Gaussian weight function

$$w_k = \exp\{-x_k^2/a^2\} / \sum_{n=1}^K \exp\{-x_n^2/a^2\}. \quad (5)$$

Here x_k is the distance between the cap center and the conversion point of the k^{th} event. The Gaussian width parameter, a , was set to be the same as the cap radius. We chose $N = 4$ to reduce uncorrelated noise relative to the usual linear stack ($N = 1$). Since the N^{th} -root stacking took account of both amplitude and coherence of the conversional signals, we expected it to be less sensitive to noise with anomalously large amplitude that might be present in some receiver function data than the linear stack. We also noticed that the N^{th} -root stacking could introduce more suppression to conversions from structures that dip

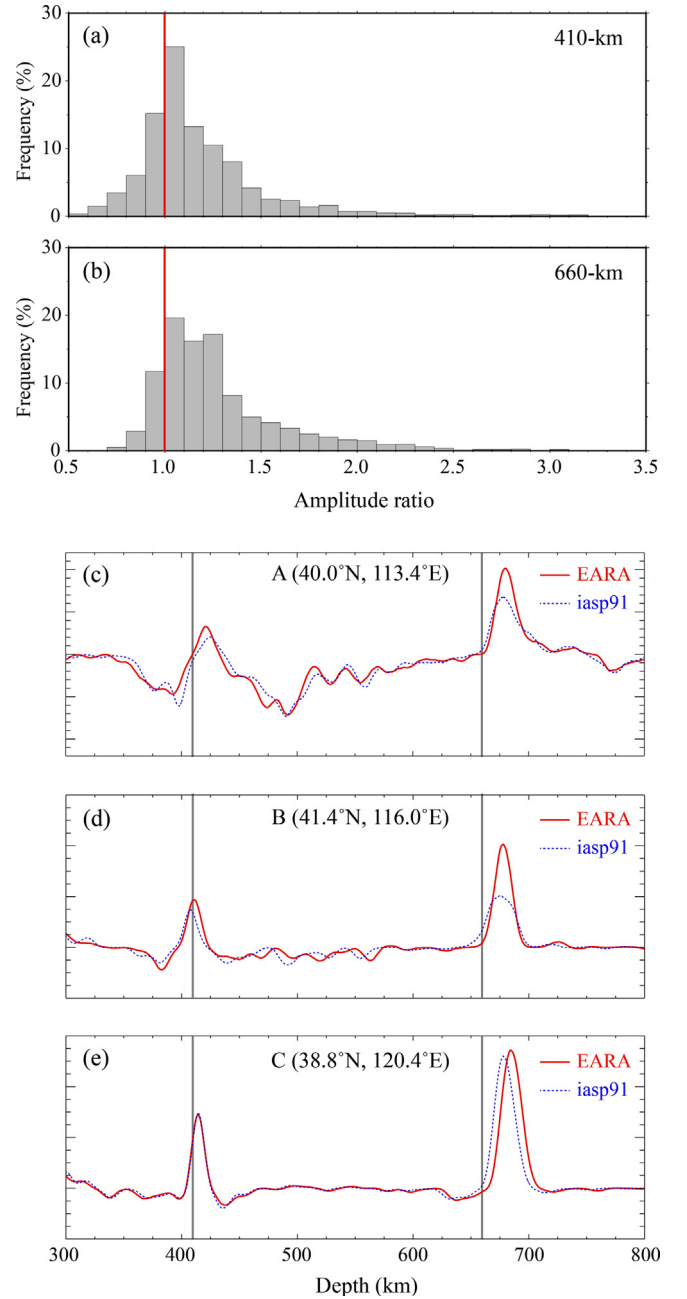


Fig. 4. (a) Histogram showing the amplitude ratio of $P410s$ migrated from 3-D and 1-D reference models. The red vertical line indicates an amplitude ratio of 1. (b) The same as (a) except for $P660s$. The average values of the two ratios are approximately 1.3. (c) Migrated P-to-S conversion amplitude at point A inside the Datong volcanic field is shown as a function of depth. Red solid and blue dotted lines represent the 3-D and 1-D migrations, respectively. The two vertical lines show the depths of 410 km and 660 km, respectively. (d) and (e) are similar to (c) except for grid points B and C inside the NY and BS transition zone anomaly regions, respectively. Note that while $P660s$ showed significant increase in (c)–(e) with the 3-D Pds moveouts, the amplitude increase of $P410s$ is rather trivial in these three examples, which is not representative of all the 2736 grids. (For interpretation of the references to color in this figure legend, the reader is referred to the web version of this article.)

significantly away from the horizontal. Fig. 3 showed five depth sections of stacked receiver functions using the 3-D Pds moveout table along latitude 38°N, 39°N, 40°N, 41°N, and 42°N, respectively.

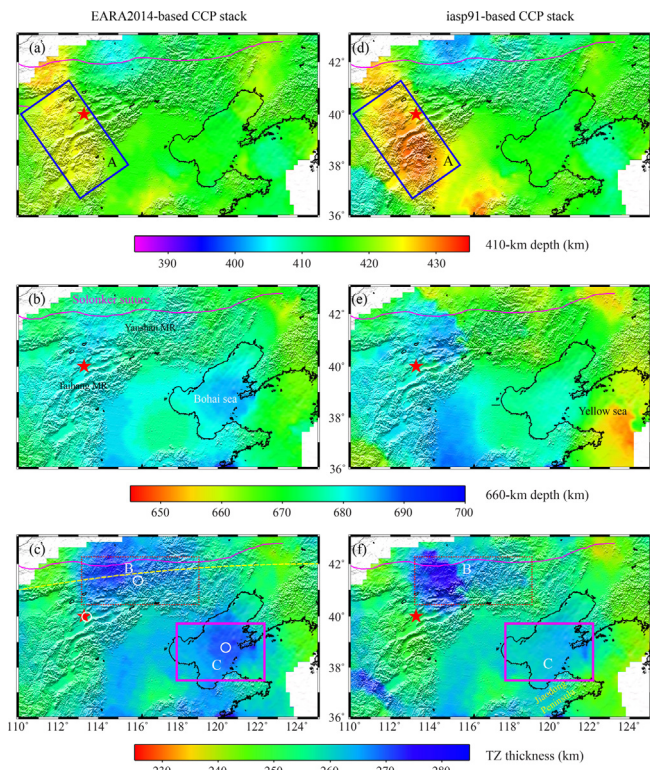


Fig. 5. Maps showing the lateral variations of depth to the 410-km (a), the 660-km (b), and the transition zone thickness (c) migrated from the 3-D EARA2014 model (Chen et al., 2015). The red star indicates the Datong volcano. The blue solid rectangle in (a), the red dotted rectangle in (c) and the pink solid rectangle in (c) represent the Datong volcanic region, the NY and BS transition zone anomalies, respectively. The pink solid line denotes the Solonker suture and the yellow dashed line shows the part of the location of the velocity profile shown in Fig. 7a. (d), (e) and (f) are the 1-D migration results, which are plotted similarly to (a), (b), and (c), respectively. (For interpretation of the references to color in this figure legend, the reader is referred to the web version of this article.)

3. Results and discussion

Fig. 3 shows that both the 410-km and 660-km discontinuities can be clearly seen from the depth sections. We also stacked the receiver functions with the 1-D *P_d* moveout table, and found that the amplitudes of the *P₄₁₀*s and *P₆₆₀*s from the 3-D migration are approximately 30% higher than those of the 1-D stacks (Fig. 4a and 4b). This suggests that the 3-D P- and S-wave velocities of the EARA2014 model better represent the true velocity structures of the study area, leading to a more in-phase stacking of the P-to-S conversion signals. To further demonstrate the difference between the 1-D and 3-D migrations, we showed depth migrated profiles at three different parts of the study area in Fig. 4c–e. Amplitudes of the *P₄₁₀*s and *P₆₆₀*s from the 3-D migration in all the three profiles are larger than those of the 1-D stacking.

We manually picked the peak depths of the *P₄₁₀*s and *P₆₆₀*s from the caps that are sampled by more than 400 receiver functions. We also calculated one standard deviation (1σ) of the CCP stacked depths based on a bootstrap method (Efron and Tibshirani, 1986). The 3-D migration results of the 410-km and 660-km discontinuities and the mantle transition zone thickness are shown in Fig. 5a, 5b, and 5c, respectively. For comparison, we also showed the depth variations of the two discontinuities based on the 1-D iasp91 model and the corresponding transition zone thickness in Fig. 5d–f. We also computed 3-D *P_d*s moveouts using a more recent 3-D model, FWEA18 (Tao et al., 2018), for part of the receiver function data and conducted 3-D CCP stacking at 3 points (white circles in Fig. 5c) located in the Datong, northern

Yanshan mountain range, and the Bohai Sea regions. We found that the estimated depths of the two discontinuities based on the FWEA18 model are within the 1σ of the EARA2014 results. Thus in this paper we focused our discussion based on the EARA2014 results.

The average depth of the 410-km discontinuity estimated from the 1-D and 3-D migrations is 416.6 and 416.9 km; both are very close to the global average (418 km) obtained from global SS precursor studies (Flanagan and Shearer, 1998; Gu and Dziewonski, 2002). On the other hand, the average depth of the 660-km discontinuity from the 3-D migration is 676.3 km, 3.5 km deeper than the average of the iasp91-based stacking (672.8 km). This difference is caused by the high P- and S-wave velocity anomalies of the EARA2014 model inside the transition zone beneath the study area.

Both the 410-km and 660-km tomography showed significant differences between the 3-D and the 1-D migrations, which are shown in the left and right columns in Fig. 5, respectively. The region around the Datong volcano (blue square A in Fig. 5) showed a deepened 410-km with a maximum depth of 431 km in the 1-D image (Fig. 5d). This depression is, however, less dominant in the 3-D image (Fig. 5a) as it is largely caused by unmodeled low velocity anomalies of the 1-D model in the upper mantle beneath the area. It is clear that the difference in mantle transition zone thickness between the 1-D and 3-D models is caused by the difference of the 410-km depth (Fig. 6a). There is an anti-correlation between the changes of 410-km depth and transition zone thickness (Fig. 6a), while the correlation between the changes of 660-km depth and the transition zone thickness (Fig. 6b) is less obvious. The 1-D and 3-D migrated profiles at the Datong volcano (Fig. 4c) clearly showed that the 3-D *P₄₁₀*s and *P₆₆₀*s are of greater amplitude and narrower pulse width (red solid line), indicating better focusing in the *P_d*s migration based on more accurate movement corrections.

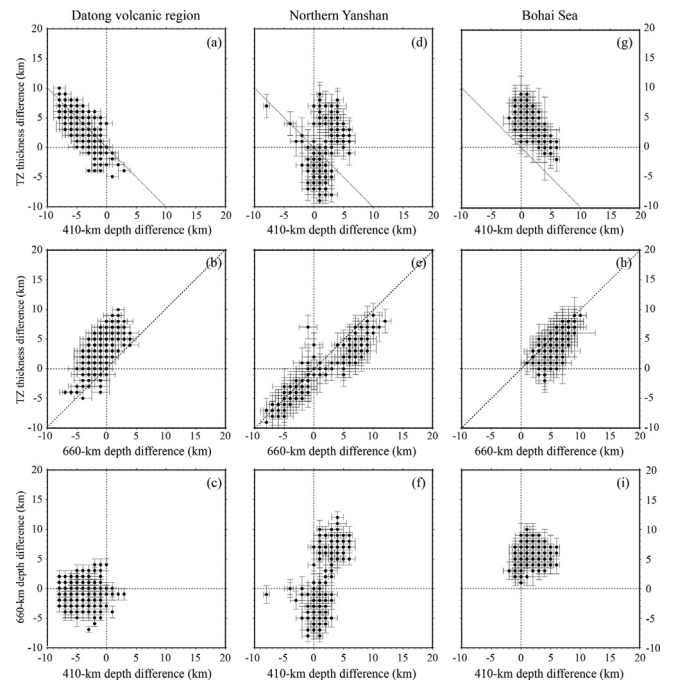


Fig. 6. (a) Differences in transition zone thickness between the 3-D and 1-D migrations measured in the Datong volcanic region are shown as a function of differences in the depth to the 410-km. Note that 1σ uncertainties are shown as error bars. The dotted line with a slope of negative one represents a perfect anticorrelation between the two datasets. (b) The same as (a) except for the 660-km, and the dotted line with a slope of positive one represents a perfect correlation between the two datasets. (c) Differences in the depth to the 660-km between the 3-D and 1-D migration are shown as a function of differences in the depth to the 410-km. (d), (e), and (f) are similar to (a), (b), and (c), respectively, except for the NY anomaly region. (g), (h), and (i) are similar to (a), (b), and (c), respectively, except for the BS anomaly region.

The average depth of the 410-km and 660-km discontinuities beneath the Datong volcanic region is 422.0 and 679.8 km, respectively. Both are slightly deeper than their averages (416.9 and 676.3 km) of the study area, but the transition zone thickness (257.8 km) is very similar to the regional average (259.4 km), suggesting there is not significant temperature anomaly in the transition zone beneath the Datong volcanic region. Hence, it is likely that the depths of the both discontinuities are overestimated as amplitude of the low velocity anomaly in the upper mantle beneath the area might still be underestimated in the EARA2014 model. If this is the case, the source of the Datong volcano is likely fed by decompression melting induced by a lithospheric delamination process, as discussed in the next section.

While the average transition zone thickness of the study area (259.4 km) is approximately 17 km thicker than the global average (~242 km) (Flanagan and Shearer, 1998; Gu and Dziewonski, 2002), there are two distinct regions with anomalously thick transition zone beneath the northern part of the Yanshan mountain range and the Bohai Sea in the 3-D migration image (rectangles B and C in Fig. 5c). Hereafter we refer them as the NY and BS transition zone anomalies, respectively. The 3-D *Pds* gather at point B inside the NY anomaly shows a significantly better focused *P660s* and a slightly higher amplitude *P410s*, suggesting that the seismic velocities inside the mantle transition zone beneath the northern Yanshan mountain range are higher than the global average. Differences in the transition zone thickness between the 3-D and 1-D migrations are caused by differences of the depth to the 660-km discontinuity (Fig. 6e). The thickened transition zone beneath the Bohai Sea in the 3-D migration (i.e., the BS anomaly) is also caused by a more depressed 660-km discontinuity, as Fig. 5b and 5e as well as Fig. 6h show a clear positive correlation between the changes in the transition zone thickness and the depth to the 660-km discontinuity. The stacked amplitude of *P410s* in this area remained almost the same while *P660s* showed a minor increase, suggesting high velocity anomalies are mainly located inside the mantle transition zone beneath the Bohai Sea.

The average depth of the 410-km and 660-km discontinuities is 412.2 and 678.7 km beneath the northern Yanshan mountain range, and 415.0 and 680.3 km beneath the Bohai Sea. The transition zone thickness beneath the two regions is 266.5 and 265.3 km, respectively, which is 7.1 and 5.9 km thicker than the regional average value (259.4 km). If the thicker transition zone beneath the two regions is caused by temperature induced depression of the 660-km discontinuity, then the estimated temperature at the base of the transition zone is ~220 K lower than the regional average assuming a Clapeyron slope of -2.8 MPaK^{-1} (Ito and Takahashi, 1989). Meanwhile, the EARA2014 model shows that the S-wave velocity is ~2.2% and 2.7% higher than the regional average beneath the northern Yanshan mountain range and the Bohai Sea, respectively. If the temperature dependence of shear velocity ($d\ln V_s/dT$) is $-1.0 \times 10^{-4} \text{ K}^{-1}$ as suggested by Stixrude and Lithgow-Bertelloni (2012), then temperature within the transition zone beneath the two areas are expected to be 220 and 270 K lower than the regional average, which is consistent with that (220 K) inferred from the Clapeyron slope.

The NY anomaly was barely covered by the receiver function study of Wang and Niu (2011), while the BS transition zone anomaly was not resolved by their study, which we attributed to the large amount of receiver function data as well as the high-resolution EARA2014 model used in this study. The 3-D model has a very strong high S-wave velocity anomaly in the lower part of the mantle transition zone beneath eastern Bohai Sea, which was interpreted as the subducted Pacific slab (Chen et al., 2015). More recently, Tao et al. (2018) found a double high-velocity layer located above and below the 660-km under the Bohai Sea, which overlaps the BS transition zone anomaly in this study. The lower part of the layer is located just below the depth of 660 km and has a higher S-wave but an almost normal P-wave velocity structure. Tao et al. (2018) suggested that the upper part of the double fast layer could be the Pacific plate that has been subducted during the past

30 Ma. However, the lower mantle part of the double fast layer could also be the delaminated cratonic lithosphere of the ENCC, as it is featured by fast P wavespeed, very fast S wavespeed, and therefore a low V_p/V_s ratio. Since the delamination occurred between Late Jurassic and Early Tertiary, therefore the thermal signature of the delaminated cratonic lithosphere is likely faded out, resulting in a velocity structure with normal P wavespeed and composition-related high S wavespeed, which is consistent with observations on the lower-mantle part of the double fast layer. Our observation of a 10–25 km depressed 660-km discontinuity suggested that the uppermost lower mantle is likely cold, therefore the double fast layer could simply have a thermal origin, and the difference in the amplitude of the P- and S-wave velocity anomaly might be due to their different sensitivity to temperature in the lower mantle.

Recent waveform tomography (Chen et al., 2015; Tao et al., 2018) and receiver function imaging (Liu et al., 2015) suggested that stagnant subduction is not pervasively observed beneath northeast China. Our migrated images also showed that transition zone thickening occurs locally in the study area. The depression of the 660-km beneath the northern Yanshan mountain range (Fig. 5b) and the NY transition zone anomaly is difficult to be explained by the current Pacific plate subduction. The area is located at the south side of the Solonker suture, which is the location of collision between the North China Craton and the Mongolian Terranes after the closure of the Paleo-Asian Ocean. In the north side of the suture, Chen et al. (2017) proposed an ongoing lithospheric delamination beneath the southern Great Xing'an Range based on a variety of seismic observations. The NY transition zone anomaly appears to be consistent with a lithospheric delamination that is also occurring beneath the south side of the suture. Fig. 7a shows a depth cross section of the 3-D P-wave velocity structure of the NECESS P model (Obayashi et al., 2011; Tang et al., 2014) along the great circle between (41°N, 110°E) and (41°N, 140°E). Location of the western half of the section is shown in yellow dashed line in Fig. 5c.

There is a high velocity anomaly in the transition zone that collocates well with the NY anomaly. This high velocity anomaly appears to be a natural extension of a westward dipping high-velocity structure in the upper mantle starting at a depth of ~200 km. The upward extension is further supported by the measured depths of the 410-km within the high-velocity anomaly (upper dashed red line in Fig. 7a), which is 412.2 km on average, ~5 km shallower than the regional average (416.9 km) and ~6 km shallower than the global average (418 km, Flanagan and Shearer, 1998). There is a gap between this high velocity structure and the current subducting Pacific plate in the east (Fig. 7a). Therefore, it is unlikely to be the western front of the subducting Pacific plate. The uplifted 410-km results in negative buoyancy, which accelerates the sinking speed of the structure. Therefore the dipping high-velocity anomaly is expected to be a relatively young structure. Hence it is unlikely to represent an old slab of the ancient Pacific plate, which tends to stagnant at the base of the transition zone, not above the 410-km discontinuity based on its density profile. Thus we interpreted the westward dipping high velocity structure as the mantle lithosphere beneath the south side of the Solonker suture that has detached from the Moho due to negative buoyancy and are sinking into the deep mantle (Fig. 7b).

The dipping angle of the high velocity structure shown in Fig. 7a is ~35°, suggesting that lithosphere started peeling off from west. Since the volcanism in the area began at Miocene (Zhang and Guo, 2016), we speculated that the detached lithosphere is sinking with a speed of 2–3 cm/yr in order for it to reach the base the transition zone within 20 Myrs. On the other hand, we noticed that westward-dipping high-velocity anomaly is not clearly shown in EARA2014 and FWEA18. We attribute this difference largely to the relatively low lateral resolution of the two models, as they were inverted from a long-wavelength dataset that have far fewer raypaths than the traveltimes dataset used in deriving the NECESS-P wave model.

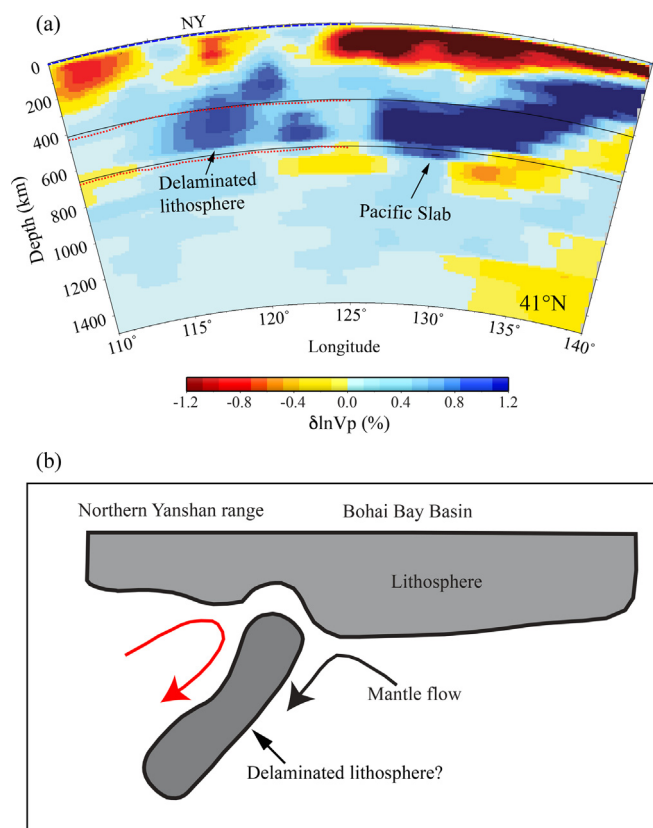


Fig. 7. (a) The 3-D NECESS P velocity model along the great circle arc between (41°N, 110°E) and (41°N, 140°E) is plotted in color contour map, with “warm” and “cool” colors indicating slow and fast velocity anomalies, respectively. Location of the western half of the depth section is denoted by the yellow dashed line in Fig. 5c. The two red dashed lines represent the 410-km and 660-km discontinuities estimated from the EARA2014 model, while the two black lines indicate the depths of 410 km and 660 km, respectively. (b) A schematic diagram showing the ongoing lithospheric delamination beneath the northern Yanshan mountain range. (For interpretation of the references to color in this figure legend, the reader is referred to the web version of this article.)

4. Conclusions

We investigated the mantle transition zone structure beneath eastern North China by migrating a large amount of receiver function data with a high-resolution 3-D P- and S-wave model. The 3-D migrated CCP images showed two regions with remarkably thickened mantle transition zone beneath the Bohai Sea and the northern Yanshan mountain range. Our observations, together with 3-D seismic velocity structure of recent tomography studies, suggest that the 660-km depression beneath the Bohai Sea is likely caused by the cold Pacific plate that has been subducted over the last 30 Ma. The thickened mantle transition zone beneath the northern Yanshan mountain range near the Solonker suture could be caused by delamination of the thickened lithosphere beneath the mountain range. The delamination also resulted in a returning upwelling that is likely feeding to the Datong volcano located slightly west to the range. Our study suggested that high-resolution 3-D velocity models are essential for imaging lateral variations of the mantle transition zone structure and for understanding deep mantle processes.

CRediT authorship contribution statement

Jiahui Zuo: Formal Analysis, Investigation, Validation, Visualization, Methodology, Writing-original draft. **Liwei Wang:** Data curation, Formal Analysis, Software, Methodology. **Fenglin Niu:**

Conceptualization, Methodology, Project Administration, Resources, Supervision, Validation, Writing - review and editing.

Declaration of Competing Interest

The authors declare that they have no known competing financial interests or personal relationships that could have appeared to influence the work reported in this paper.

Acknowledgments

We thank the Project of North China Array of the China Earthquake Administration for providing the waveform data, and Dr. Min Chen for providing the EARA2014 model. We thank the Editor and the two anonymous reviewers for their constructive comments and suggestions, which significantly improved the quality of this paper. This work was supported by the National Natural Science Foundation of China (No. 41630209).

Appendix A. Supplementary material

Supplementary data to this article can be found online at <https://doi.org/10.1016/j.jseas.2020.104266>.

References

- Chen, H., Niu, F., Obayashi, M., Grand, S.P., Kawakatsu, H., Chen, Y.J., Ning, J., Tanaka, S., 2017. Mantle seismic anisotropy beneath NE China and implications for the lithospheric delamination hypothesis beneath the southern Great Xing'an range. *Earth Planet. Sci. Lett.* 471, 32–41.
- Chen, L., Ai, Y., 2009. Discontinuity structure of the mantle transition zone beneath the North China Craton from receiver function migration. *J. Geophys. Res. Solid Earth* 114, B06307. <https://doi.org/10.1029/2008JB006221>.
- Chen, M., Niu, F., Liu, Q., Tromp, J., Zheng, X., 2015. Multi-parameter adjoint tomography of the crust and upper mantle beneath East Asia – Part I: Model construction and comparisons. *J. Geophys. Res. Solid Earth* 120, 1762–1786. <https://doi.org/10.1002/2014JB011638>.
- Chen, Y., Niu, F., Liu, R., Huang, Z., Tkalic, H., Sun, L., Chan, W., 2010. Crustal Structure beneath China from receiver function analysis. *J. Geophys. Res. Solid Earth* 115, B03307. <https://doi.org/10.1029/2009JB006386>.
- Clayton, R.W., Wiggins, R.A., 1976. Source shape estimation and deconvolution of teleseismic body waves. *Geophys. J. R. Astron. Soc.* 47, 151–177.
- Dueker, K.G., Sheehan, A.F., 1997. Mantle discontinuity structure from midpoint stacks of converted P and S waves across the Yellowstone hotspot track. *J. Geophys. Res. Solid Earth* 102, 8313–8328.
- Efron, B., Tibshirani, R., 1986. Bootstrap methods for standard errors, confidence intervals, and other measures of statistical accuracy. *Statist. Sci.* 1, 54–75.
- Fang, L.H., Wu, J.P., Lu, Z.Y., 2009. Rayleigh wave group velocity tomography from ambient seismic noise in north China. *Chin. J. Geophys.* 52, 663–671.
- Flanagan, M., Shearer, P., 1998. Global mapping of topography on transition zone velocity discontinuities by stacking SS precursors. *J. Geophys. Res. Solid Earth* 103, 2673–2692.
- Fukao, Y., Obayashi, M., Inoue, H., Nenbai, M., 1992. Subducting slabs stagnant in the mantle transition zone. *J. Geophys. Res. Solid Earth* 97, 4809–4822.
- Fukao, Y., Widiyantoro, S., Obayashi, M., 2001. Stagnant slabs in the upper and lower mantle transition region. *Rev. Geophys.* 39, 291–323.
- Gao, S., Rudnick, R.L., Carlson, R.W., McDonough, W.F., Liu, Y.S., 2002. Re-Os evidence for replacement of ancient mantle lithosphere beneath the North China craton. *Earth Planet. Sci. Lett.* 198, 307–322.
- Grand, S.P., 2002. Mantle shear-wave tomography and the fate of subducted slabs. *Philosop. Trans. Royal Soc. A* 360 (1800), 2475–2491.
- Grand, S.P., Helmberger, D.V., 1984. Upper mantle shear structure of North America. *Geophys. J. Int.* 76 (2), 399–438.
- Griffin, W.L., Zhang, A., O'Reilly, S.Y., Ryan, C.G., 1998. Phanerozoic evolution of the lithosphere beneath the Sino-Korean craton. In: Flower, M.F.J., Chung, S.-L., Lo, C.-H., Lee, T.-Y. (Eds.), *Mantle dynamics and plate interactions in East Asia*. American Geophysical Union, pp. 107–126.
- Gu, Y.J., Dziewonski, A.M., 2002. Global variability of transition zone thickness. *J. Geophys. Res. Solid Earth* 107, 2135. <https://doi.org/10.1029/2001JB000489>.
- Guan, Z., Niu, F., 2018. Using fast marching eikonal solver to compute 3D Pds traveltimes for deep receiver-function imaging. *J. Geophys. Res. Solid Earth* 123, 9049–9062. <https://doi.org/10.1029/2018JB015892>.
- Huang, J., Zhao, D., 2006. High-resolution mantle tomography of China and surrounding regions. *J. Geophys. Res.* 111, B09305. <https://doi.org/10.1029/2005JB004066>.
- Ito, E., Takahashi, E., 1989. Postspinel transformations in the system Mg₂SiO₄-Fe₂SiO₄ and some geophysical implications. *J. Geophys. Res.: Solid Earth* 94, 10637–10646.
- Katsura, T., Ito, E., 1989. The system Mg₂SiO₄-Fe₂SiO₄ at high pressures and temperatures: precise determination of stabilities of olivine, modified spinel, and spinel. *J.*

- Geophys. Res. Solid Earth 94, 15663–15670.
- Kennett, B.L.N., Engdahl, E.R., 1991. Travel times for global earthquake location and phase identification. *Geophys. J. Int.* 105, 429–465.
- Liu, Z., Niu, F., Chen, Y.J., Grand, S.P., Kawakatsu, H., Ning, J., Tanaka, S., Obayashi, M., Ni, J., 2015. Receiver function images of the mantle transition zone beneath NE China: new constraints on intraplate volcanism and deep subduction. *Earth Planet. Sci. Lett.* 412, 101–111.
- Lu, L.Y., He, Z.Q., Ding, Z.F., Yao, Z.X., 2009. Investigation of ambient seismic noise sources in the North China Array. *Chin. J. Geophys.* 52, 1053–1060.
- Megnin, C., Romanowicz, B., 2000. The three-dimensional shear velocity structure of the mantle from the inversion of body, surface and higher-mode waveforms. *Geophys. J. Int.* 143 (3), 709–728.
- Menzies, M.A., Fan, W.-M., Zhang, M., 1993. Paleozoic and Cenozoic lithoprobes and the loss of > 120 km of Archean lithosphere, Sino-Korean craton, China. In: Prichard, H.M., Alabaster, T., Harris, N.B.W., Neary, C.R. (Eds.), *Magmatic Processes and Plate Tectonics*. Geological Society, London, pp. 71–81.
- Muirhead, K.J., 1968. Eliminating false alarms when detecting seismic events automatically. *Nature* 217, 533–534.
- Niu, F., Kawakatsu, H., 1998. Determination of the absolute depths of the mantle transition zone discontinuities beneath China: Effect of stagnant slabs on mantle transition zone discontinuities. *Earth Planets Space* 50, 965–975.
- Niu, F., Levander, A., Ham, S., Obayashi, M., 2005. Mapping the subducting Pacific slab beneath southwest Japan with Hi-net receiver functions. *Earth Planetary Sci. Lett.* 239, 9–17.
- Niu, F., Li, J., 2011. Component azimuths of the CEArray stations estimated from P-wave particle motion. *Earthq. Sci.* 24, 3–13.
- Obayashi, M., Kawakatsu, H., Tanaka, S., Chen, Y.J., Ning, J., Grand, S.P., Niu, F., Miyakawa, K., Idehara, K., Tonegawa, T., Iritani, R., 2011. P-wave tomography of Northeastern China observed with NECESSArray, Abstract S24B-06, Fall Meeting, American Geophysical Union, San Francisco, California, 5–9 December.
- Obayashi, M., Yoshimitsu, J., Nolet, G., Fukao, Y., Shiobara, H., Sugioka, H., Miyamachi, H., Gao, Y., 2013. Finite frequency whole mantle P wave tomography: Improvement of subducted slab images. *Geophys. Res. Lett.* 40, 5652–5657. <https://doi.org/10.1002/2013GL057401>.
- O'Reilly, S.Y., Griffin, W.L., Poudjom Djomani, Y.H., Morgan, P., 2001. Are lithospheres forever? Tracking changes in subcontinental lithospheric mantle through time. *GSA Today* 11, 4–10.
- Stixrude, L., Lithgow-Bertelloni, C., 2012. Geophysics of chemical heterogeneity in the mantle. *Annu. Rev. Earth Planet. Sci.* 40, 569–595.
- Tang, Y., Obayashi, M., Niu, F., Grand, S.P., Chen, Y.J., Kawakatsu, H., Tanaka, S., Ning, J., Ni, J., 2014. Changbaishan volcanism in northeast China linked to subduction-induced mantle upwelling. *Nat. Geosci.* 7, 470–475. <https://doi.org/10.1038/ngeo2166>.
- Tao, K., Grand, S.P., Niu, F., 2018. Seismic structure of the upper mantle beneath Eastern Asia from full waveform seismic tomography. *Geochem. Geophys. Geosyst.* 19. <https://doi.org/10.1029/2018GC007460>.
- Vinnik, L.P., 1977. Detection of waves converted from P to SV in the mantle. *Phys. Earth Planet. Inter.* 15, 39–45.
- Walck, M.C., 1984. The P-wave upper mantle structure beneath an active spreading centre: the Gulf of California. *Geophys. J. Int.* 76, 697–723.
- Wang, X., Ding, Z., Zhu, L., 2016. Lithospheric structure of the northeastern North China craton imaged by S receiver functions. *Pure Appl. Geophys.* 173, 2727–2736.
- Wang, X., Niu, F., 2011. Imaging the mantle transition zone beneath eastern and central China with CEArray receiver functions. *Earthq. Sci.* 24, 65–75.
- Windley, B.F., Maruyama, S., Xiao, W.J., 2010. Delamination/thinning of sub-continental lithospheric mantle under Eastern China: The role of water and multiple subduction. *Am. J. Sci.* 310, 1250–1293.
- Zhang, M., Guo, Z., 2016. Origin of Late Cenozoic Abaga-Dalinuoer basalts, eastern China: Implications for a mixed pyroxenite–peridotite source related with deep subduction of the Pacific slab. *Gondwana Res.* 37, 130–151.
- Zheng, X.F., Ouyang, B., Zhang, D.N., Yao, Z.X., Liang, J.H., Zheng, J., 2009. Technical system construction of Data Backup Centre for China Seismograph Network and the data support to researches on the Wenchuan earthquake. *Chin. J. Geophys.* 52, 1412–1417. <https://doi.org/10.3969/j.issn.0001-5733.2009.05.031>.
- Zhu, H., Bozdag, E., Peter, D., Tromp, J., 2012a. Structure of the European upper mantle revealed by adjoint tomography. *Nat. Geosci.* 5, 493–498. <https://doi.org/10.1038/ngeo1501>.
- Zhu, R.X., Yang, J.H., Wu, F.Y., 2012b. Timing of destruction of the North China Craton. *Lithos* 149, 51–60.